Role of Glycosphingolipid Conformational Change in Membrane Pore Forming Activity of Cobra Cardiotoxin†

Siu-Cin Tjong,‡ Po-Long Wu,§ Chang-Mao Wang,‡ Wei-Ning Huang,|| Nan-Lu Ho,‡ and Wen-guey Wu*,‡,§

Institute of Bioinformatics and Structural Biology, National Tsing Hua University, National Synchrotron Radiation Research Center, and Yuan Pei University, Hsinchu, Taiwan

Received May 8, 2007; Revised Manuscript Received August 24, 2007

ABSTRACT: The major cardiotoxin from Taiwan cobra (CTX A3) is a pore forming β-sheet polypeptide that requires sulfatide (sulfogalactosylceramide, SGC) on the plasma membrane of cardiomyocytes for CTX-induced membrane leakage and cell internalization. Herein, we demonstrate by fluorescence spectroscopic studies that sulfatides induce CTX A3 oligomerization in sulfatide containing phosphatidylcholine (PC) vesicles to form transient pores with pore size and lifetime in the range of about 30 Å and 10^{-2} s, respectively. These values are consistent with the CTX A3-induced conductance and mean lifetime determined previously by using patch−clamp electrophysiological experiments on the plasma membrane of H9C2 cells. We also derived the peripheral binding structural model of CTX A3−sulfatide complex in sulfatide containing PC micelles by NMR and molecular docking method and compared with other CTX A3-sulfatide complex structure determined previously by X-ray in membrane-like environment. The NMR results indicate that sulfatide head group conformation changes from a bent shovel (*−sc/ap*) to an extended (*sc/ap*) conformation upon initial binding of CTX A3. An additional global reorientation of sulfatide molecule is also needed for CTX A3 dimer formation as inferred by the difference between the X-ray and NMR complex structure. Since the overall folding of CTX A3 molecules remained the same, sulfatide in phospholipid bilayer is proposed to play an active role by involving its local and global conformational changes to promote both the oligomerization and reorientation of CTX A3 molecule for its transient pore formation and cell internalization.

The structure and dynamics of protein−lipid interaction on the membrane surface is important to understand the molecular mechanisms of an antibiotic polypeptide to form pores and kill bacteria (*1*−*3*), of a fusogenic protein to induce cell fusion (*4*−*6*), of a cell penetrating polypeptide to deliver cargo across plasma membrane (*7*, *8*) and an ion channel to gate and control membrane potential (*9*−*11*). Recent advancement in structural biology has indeed shed much light to determine the three-dimensional structures of both integral and peripheral membrane proteins (*12*−*15*) and how these proteins could undergo global conformational change upon protein−membrane interaction and become stabilized within lipid bilayers (*16*−*19*). In addition, analysis of the amino acid distribution on membrane protein structure has revealed a crucial role for aromatic amino acid residues such as Trp and Tyr, and positively charged residues like Arg and Lys in anchoring and snorkeling the proteins along the bilayer surface during membrane translocation process (*20*, *21*). However, computer simulations on polypeptide getting inserted into lipid bilayer further reveal that lipid should be considered as an extended part of protein (*22*−*24*). Hence, it is important to determine both the protein and lipid structure to understand its processing events.

Cobra cardiotoxins (CTXs[1]), a family of basic polypeptides having lipid (*25*, *26*) and heparin binding (*27*−*29*) capability similar to the cell-penetrating polypeptides, have recently been demonstrated to form pores in cardiomyocyte plasma membrane (*30*) and anionic lipid containing model membrane (*31*, *32*). Specifically, monoclonal anti-sulfatide IgM O4 and IgG Sulf1 are capable of inhibiting the action of CTX A3 (the major CTX from Taiwan cobra venom) on cardiomyocytes by preventing CTX A3-induced membrane leakage and cell internalization (*30*). The interaction of CTX A3 with negatively charged lipid causes CTX dimerization, an important intermediate for the eventual oligomerization of CTX during CTX pore formation (*32*). Since CTX A3 is an

† This work was funded by National Science Council, Taiwan, to W.-g.W.

* To whom correspondence should be addressed: National Synchrotron Radiation Research Center and Institute of Bioinformatics and Structural Biology, National Tsing Hua University, Hsinchu 30043, Taiwan. Tel: 886-3-578-3810. Fax: 886-3-578-3815. E-mail: wgwu@nsrrc.org.tw.

‡ National Tsing Hua University.

§ National Synchrotron Radiation Research Center.

|| Yuan Pei University.

[1] Abbreviations: 6-CF, 6-carboxyfluorescein; CTX, cardiotoxin; DPC, dodecylphosphocholine; DQF-COSY, double quantum filtered correlation spectroscopy; FD-4 and FD-70, fluorescently labeled dextrans; FTIR, Fourier transform infrared; GalCer, galactosyl ceramide; Gal3S, galactose-3-sulfate; HFA-SGC, hydroxylated fatty acids sulfatide; LPC, 1-myristoyl-2-hydroxy-*sn*-glycero-3-phosphocholine; NFA-SGC, non-hydroxylated fatty acids sulfatide; NMR, nuclear magnetic resonance; NOE, Nuclear overhauser effect; NOESY, nuclear Overhauser effect spectroscopy; POPS, 1-palmitoyl-2-oleoyl-*sn*-glycero-3-phospho-L-serine; POPC, 1-palmitoyl-2-oleoyl-*sn*-glycero-3-phosphocholine; POPG, 1-palmitoyl-2-oleoyl-*sn*-glycero-3-phospho-*rac*-1-glycerol; Rh-CTX, rhodamine-labeled cardiotoxin; SDS, sodium dodecyl sulfate; SGC, sulfogalactosylceramide/sulfatide; TOCSY, total correlation spectroscopy.

10.1021/bi700871x CCC: $37.00
Published on Web 10/06/2007

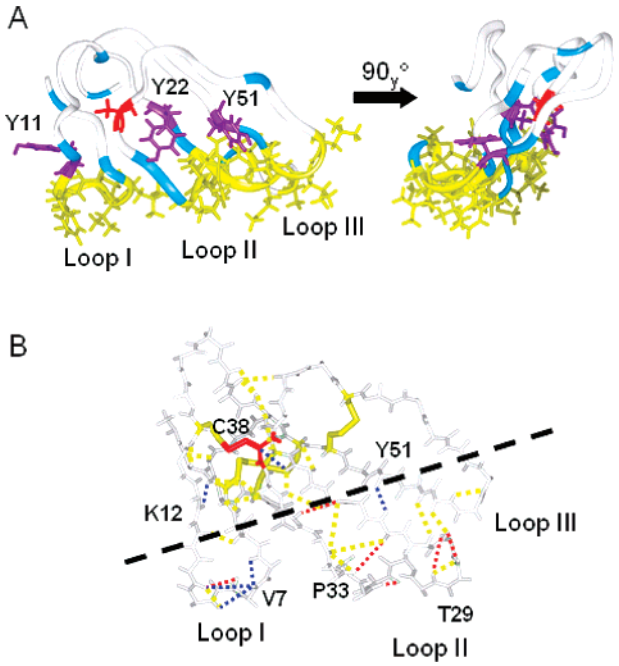

FIGURE 1: Three-fingered amphiphilic CTX A3 molecule (PDB ID: 1HOJ, *32*) shown its convex side (left panel) and after 90y° rotation (right panel) in ribbon representation (A) and stick model representation (B) to emphasize its rigid structure tightened by four disulfide bonds. In panel A, the amino acid residues possibly involved in membrane interaction are shown in stick model. Hydrophobic residues are colored yellow, positively charged residues are colored blue, polar Tyr residues are colored purple, and the Cys 38 residue that is crucial in negatively charged ligand interaction is colored red. In panel B, the four pairs of disulfide bond (Cys 3−Cys 21, Cys 14−Cys 38, Cys 42−Cys 53, Cys 54−Cys 59, colored as yellow sticks) and the invariant NMR NOE connectivities (dashed yellow line) are shown to preserve its global folding and maintain the extended five stranded β-sheet structure before and after mixed micelle interaction. The major conformational changes are identified mainly at the tips of the three-fingered loops as emphasized by the observed change in NOE connectivities colored by dashed blue and red lines. Dashed blue and red lines represent newly detected and disappeared NOE of CTX A3 molecule after CTX A3 bound to SGC/DPC micelles, respectively. Black line depicts the interface region for CTX A3 binding peripherally to the membrane surface with the three hydrophobic loops inserted into the hydrophobic regions of lipid bilayers.

amphiphilic three-fingered polypeptide with basic Lys and aromatic Tyr flanking the three hydrophobic loops (Figure 1A), CTX A3 has also been demonstrated binding to membrane surface peripherally (*31*). Such a binding prototype is also consistent with the notion that Tyr and Lys amino acid residues may function as an anchor at the interface of lipid bilayers for a membrane protein. It is therefore intriguing to see how the CTX A3 could form pores in the membrane bilayer, considering the CTX A3 molecule as a rigid molecule consisting of four disulfide bonds (Figure 1B) to prevent global conformational change of the protein during the pore forming process. One of the likely models to explain the process is the toroidal model (recently modified as distorted toroidal or protein aggregate model, *33*) that requires lipid rearrangement to facilitate the protein insertion (*34*, *35*).

CTX A5, a noncytotoxic CTX homologue capable of peripheral binding to phospholipid bilayer in a similar fashion to CTX A3 (*26*, *36*), does not induce membrane leakage (*32*). CTX A5 consists of more extended continuous hydrophobic loops to allow its binding to lipid bilayers, and the only CTX consisting of Phe 22, instead of Tyr 22, with reduced hydrogen-bonding capability at the core region (Figure 2A). The lipid-induced oligomerization ability of CTX A5 seems to be compromised as compared to that of CTX A3 (*32*). It has been suggested that Met 24 and Met 26 in CTX A3 play a role in mediating the dimer formation in specific form, when these amino acid residues are mutated into Ala 24 and Leu 26, respectively, in CTX A5 (*32*). It is therefore interesting to study the sulfatide-dependent pore formation of CTX A3 and A5 in model membranes and examine its specificity as compared to other anionic lipids. Just as the pore formation processes of antimicrobial polypeptides require PG for its action on the bacterial cell surface (*37*, *38*), sulfatide (SGC) is the only glycosphingolipid molecule known to be present at the outer leaflet of plasma membranes to induce the action of CTX A3 (*30*).

Three-dimensional (3D) structures of many CTX homologues have been determined by NMR and X-ray method (see ref *39* for a summary of the available structures). Three-fingered loop folding topology with a large triple-stranded antiparallel and a short double-stranded β-sheet has been preserved for all the studied CTX homologues interacting with phospholipid, including CTX Tγ, CTX O2, CTX A5 and A3, based on the distance geometric constraint established by NMR NOE approach (*40*−*43*). The effect of lipid or heparin binding to CTXs on its 3D structures has also been studied by using lyso-phosphatidylcholine (LPC) micelles and heparin-derived short chain mimetics (*43*). The tripartite interaction study of CTX A3 with heparin-derived mimetics and LPC micelles did imply a delicate conformational change near its membrane binding loops due to the structural coupling between the connecting loops and its β-strands (*43*). Since heparin-derived short chain mimetics are found to bind to CTX A3 at the anionic pocket of the rigid core region with the additional help of hydrogen bond formation via OH of Tyr 22 and NH of Cys 38 (Figure 1, *44*), it was suggested that heparin binding to CTX A3 may stabilize its membrane-bound form through the proposed structural change. SGC molecule is a sulfated glycoconjugate with an anionic headgroup moiety similar to heparin mimetics and two hydrophobic lipid chains to form membrane bilayer. It would be interesting to study how SGC interact with CTXs.

We have previously determined the crystal CTX A3/SGC complex structure in a membrane-like environment to understand the action mechanism of CTX A3 (*30*). The orientation of the SGC fatty acyl chains in CTX A3/SGC X-ray structure is found unexpectedly to flip 180° opposite to the presumed membrane binding orientation of the three hydrophobic loops (*31*, *32*, *43*). It was therefore proposed that CTX A3/SGC complex structure may represent the insertion mode of CTX A3 within the lipid bilayer and play a role in promoting CTX A3 dimerization and insertion into lipid bilayers. The structure of CTX A3/SGC complex upon its initial peripheral binding at the membrane surface, however, is not available. In this study, the question is addressed using NMR. We also characterize the property of CTX A3 pore in SGC containing vesicles by using fluorescence spectroscopy and demonstrate the similarity of CTX A3 pore formation in plasma and model membranes. The results indicate that glycosphingolipid conformational changes

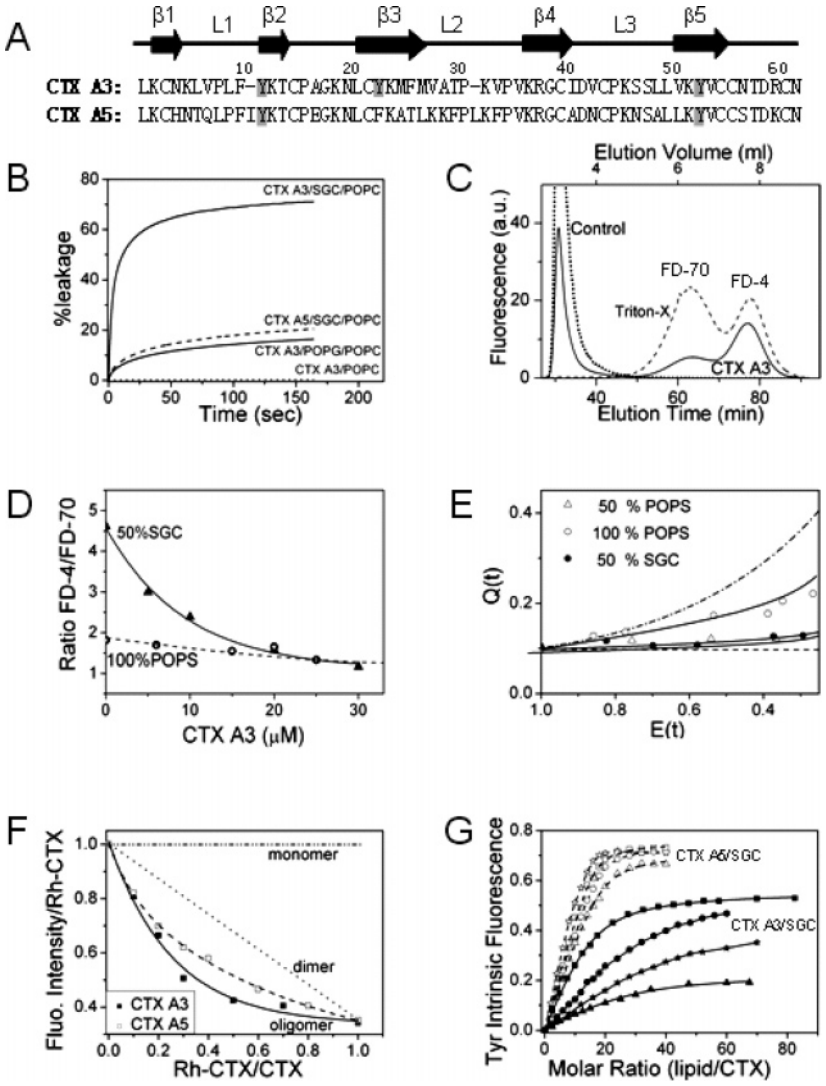

FIGURE 2: Fluorescence spectroscopic investigation on the membrane pore forming activities of CTX A3 in model membrane: (A) Pairwise sequence alignment of CTX A3 and A5 with the secondary structural elements listed. (B) CTXs-induced leakage of 6-CF vesicles of different lipid component plotted as a function of time after adding CTXs. Mixed vesicles were prepared by mixing equal molar of SGC or POPG into POPC lipid. Concentrations of CTXs and vesicle were 0.16 and 10 μM, respectively. (C) Elution profiles for the CTX A3 treated 50% SGC containing POPC vesicles with co-encapsulated fluorescence markers of different size (FD-4 and FD-70). (D) The different selectivity on leakage marker size of SGC/POPC and pure POPS vesicles. (E) Transient quenching factor Q versus efflux function E curves for vesicles with designated lipid compositions. The dashed lines indicate the two extreme cases of $\rho = 0$ ("all-or-none" mode of efflux, horizontal line) and $\rho \rightarrow 1$ (upper bound of graded efflux). The two solid curves for $\rho = 0.26$ and $\rho = 0.1$ are fits to the experimental data obtained with POPS and SGC/POPC vesicles, respectively. (F) Fluorescence spectra of a fixed and variable ratio of rhodamine B-conjugated CTX A3 and CTX A5 in the presence of SGC large unilamellar vesicles. Dash-dotted line and dotted line are simulated curve of monomers and dimer respectively. Oligomeric curve of CTX A5 is represented by dashed line, open square; while solid line, close square represent oligomeric curve of CTX A3. (G) Change in intrinsic fluorescence intensity of Tyr (residues shaded in gray in (A)) of CTX A3 (closed symbols) and CTX A5 (open symbols) plotted against molar ratio of lipid/CTX. CTXs were titrated with elevated ratio of SGC/LPC micelle: 0% SGC/100% LPC (triangle); 1% SGC/99% LPC (star); 5% SGC/95% LPC (circle); and 10% SGC/90% LPC (square). Titration curves were fitted as follows: $K_d = 74$ μM, $n = 26$ for CTXA3/LPC; $K_d = 33$ μM, $n = 15$ for CTXA3/10% SGC/LPC; $K_d = 12$ μM, $n = 18$ for CTXA5/LPC; $K_d = 6$ μM, $n = 16$ for CTXA5/10% SGC/LPC.

play an important factor for CTX A3 binding and dimer formation to account for its pore formation. SGC should be considered as an extension part of the CTX A3 molecule during membrane translocating process.

MATERIALS AND METHODS

Materials and Purification. The dodecylphosphocholine (DPC), brain-sulfatides (SGC), 1-palmitoyl-2-oleoyl-*sn*-glycero-3-phosphocholine (POPC), 1-palmitoyl-2-oleoyl-*sn*-glycero-3-phospho-*rac*-1-glycerol (POPG), 1-myristoyl-2-hydroxy-*sn*-glycero-3-phosphocholine (LPC), and 1-palmitoyl-2-oleoyl-*sn*-glycero-3-phospho-L-serine (POPS) were obtained commercially from Avanti Polar Lipids. The SGC used was a mixture purified from porcine brain which contain both hydroxylated fatty acids (HFA-SGC) and nonhydroxylated fatty acids (NFA-SGC), and the ratio between NFA and HFA is approximately 1:0.3−0.8 (*45*). Deuterium-labeled dodecylphosphocholine (d_{38}-DPC) was bought from Cambridge Isotope Laboratories. Galactose-3-sulfate (Gal3S) was synthesized and kindly provided by Dr. Dennis M. Whitfield, NRC, Canada. Rhodamine B isothiocyanate, fluorescently labeled dextrans FD-4 and FD-70, and 6-carboxyfluorescein (6-CF) were purchased from Sigma Chemical Co. CTX A3 and CTX A5 were purified by SP-Sephadex C-25 ion

exchange chromatography followed by HPLC on a reverse phase C-18 column from crude venom of *Naja atra* (Snake's education farms, Tainan, Taiwan) previously described (*36*).

Vesicle and Micelle Preparation. Desired ratios of lipids were dried under vacuum overnight and then hydrated with buffer. The suspension was frozen and thawed several times and was successively extruded through a polycarbonate filter with the pore size of 0.1 μm for obtaining homogeneous large unilamellar vesicles. For micelle preparation no extrusion through filter was needed. For the pore size determination experiments, extra compositions of 2 mg/mL FD-4 and 4 mg/mL FD-70 were added in the buffer (*46*). Vesicles used in fluorescence-leakage experiments were formed in the presence of 10 mM Tris (pH 7.4), 75 mM NaCl, and 50 mM 6-carboxyfluorescein (6-CF). Sepharose CL-4B column was used to remove the residual fluorescent molecules outside of the vesicles, and the lipid concentration was determined by inorganic phosphate assay as described (*47*).

Vesicle Leakage and Pore Lifetime Calculation. Release of vesicle contents was detected by 6-CF fluorescence intensity on an SLM-4800 fluorescence spectrometer. Although 6-CF displays low fluorescence intensity at high concentration, its intensity increases sharply at low concentrations. Vesicles containing 6-CF were incubated at a final volume of 1 mL of buffer in a 1 × 1 cm quartz cuvette. After the addition of CTX, the fluorescence intensity was monitored as a function of time for the CTX-induced vesicle leakage process. The 6-CF leakage was calculated using the following expression: % leakage = $(F_t - F_i)/(F_f - F_i)$, where F_i is the initial fluorescence before adding proteins, F_t is the fluorescence reading at time t, and F_f is the final fluorescence determined by adding Triton 0.02% (*26*). The excitation and emission wavelengths were 480 and 520 nm, respectively. For transient pore lifetime calculation, by using vesicle-entrapped CF concentration versus fluorescence static quenching standard curves (*48*) and the toxin-induced transient quenching factor (Q_t), the value of single-pore retention factor ρ can be fitted by $E(t)-Q_t$ curve (*49*). The average lifetime of the toxin-induced pore formation can then be decided based on the known size of vesicle.

Pore Size Determination. Fluorescein dextran containing vesicles (1.2 mM and 50 μL) were treated either with Triton X-100, to determine the ratio of entrapped molecules, or with CTX A3, to examine differential molecule release. After 20 min, treated vesicle was applied to a 45 × 0.5 cm CL-4B column with an elution rate of 6 mL/h. The elution profile was determined by a Hitachi F1050 fluorescence spectrophotometer. Excitation and emission wavelengths were 490 and 530 nm, respectively. To estimate the fraction of released molecules, a best-fit Gaussian curve was used to determine the area of elution profiles. When the leakage fraction was relatively small and the best-fit Gaussian curve was difficult to obtain, the leakage fraction was determined by the peak height of elution profile. We assume that the released fraction corresponds to $I_i = I_{oi}(1 - \exp(-R_i))$ where I_i, I_{oi}, and R_i were the released amount, total amount, and intrinsic leakage factor of different marker i, respectively.

Fluorescence Labeling on CTX. CTX (0.2 mM) was mixed with rhodamine B isothiocyanate (0.4 mM) in the presence of 100 mM phosphate buffer (pH 7.4) containing 6 M guanidine-HCl. The reaction mixture was incubated at room temperature for 12 h, and the resulting fluorescence-conjugated CTX was purified by HPLC. Single fluorescent probe-conjugated CTX was further identified using electrospray ionization mass spectrometry (Quatro Ultima, Micro-Mass). For characterization of the conjugated position on CTX, the sample was dissolved in 100% trifluoroacetic acid at 40 °C for 20 min to obtain conjugated amino acids of CTX and the subsequent molecular weight verified by mass spectrometry. Concentrations of fluorescence-labeled and unlabeled CTX were determined using extinction coefficients of $\epsilon^{558} = 105{,}000\ M^{-1}\ cm^{-1}$ for rhodamine B-conjugated CTX A3, $\epsilon^{276} = 4185\ M^{-1}\ cm^{-1}$ for CTX A3, and $\epsilon^{276} = 2813\ M^{-1}\ cm^{-1}$ for CTX A5. For each experiment, only N-terminal fluorescence-conjugated CTXs were used.

CTX Oligomerization by Fluorescence Homotransfer Measurement. The steady-state fluorescence spectra for the determination of CTX oligomerization upon binding to anionic lipids were obtained on an SLM-4800 fluorescence spectrometer with excitation and emission wavelengths set at 550 and 580 nm, respectively. Fluorescence-labeled and unlabeled CTX were mixed in an appropriate molar ratio in the presence of 10 mM Tris buffer (pH 7.4) containing 150 mM NaCl. The final concentration of both proteins was maintained at 0.1 μM. Upon the addition of anionic lipid vesicles (30 μM) to fluorescence-labeled CTX, the fluorescence intensity spontaneously decreased as a result of the fluorescence energy homotransfer (self-quenching) during the oligomerization process. The effect of self-quenching became less if the intrinsic CTX was added to dilute the fluorescence-labeled CTX (*50*, *51*). All experiments were performed at 25 °C.

Binding Isotherm by Intrinsic Fluorescence Measurements. Intrinsic fluorescence intensities of Tyr of CTXs were monitored to determine binding isotherm of the toxin with SGC/LPC or POPG/LPC mixed micelles or pure LPC micelles of various ratios. The excitation and emission wavelengths were set at 280 and 310 nm, respectively, by using a SLM 4800 fluorescence spectrometer. Known concentration of CTX was titrated as a function of increasing lipid concentration. 50 mM Tris buffer containing 150 mM NaCl was used, pH was adjusted to pH 7.4, and a temperature of 25 °C was used throughout all experiments. Binding data were analyzed according to our previous study (*36*). The dissociation constant, K_d, was simulated by nonlinear least-squares fitting of data according to eq 1.

$$K_d = \frac{([P]_t - [PL_n])([L]_t - n[PL_n])}{[PL_n]} \qquad (1)$$

$[P]_t$ and $[L]_t$ are the total concentrations of CTX and LPC, respectively. $[PL_n]$ represents the concentration of lipid−protein complexes, which was estimated by the change of fluorescence intensity. The n value represents the number of lipid molecules to constitute a CTX binding site.

NMR Spectroscopy and Chemical Shift Variation Analysis. The NMR samples were prepared by dissolving 1 mM CTX in 500 μL of 10% D_2O/90% H_2O or 100% D_2O mixture with 10 mM phosphate buffer. The desired amount and ratio of lipid micelle or Gal3S was added into the sample. Saturated ratios of CTX/lipid 1 mM/50 mM were used throughout lipid micelle experiments, while an excess ratio of CTX/Gal3S 1 mM/17 mM was used for CTX/Gal3S binding experiments. The pH of the sample was adjusted to 6.0 ± 0.1 by titrating

with NaOH and HCl. For simplicity, deuterium labeled DPC (d_{38}-DPC) was used for the chemical shift perturbation experiments.

Two-dimensional DQF-COSY, TOCSY (90 ms mixing time), and NOESY (150 ms mixing time) experiments (*52*) were recorded on a Bruker DMX500 spectrometer equipped with a 5 mm triple resonance probe. Water suppression was achieved by pulsed field gradient with the 3−9−19 WATERGATE sequence. The NMR experiments for the sample of CTX/Gal3S and CTX/lipid micelle mixture were performed at 27 and 45 °C, respectively. Higher temperature was used for CTX A3/lipid micelle mixture because of the broader NMR line width and the apparent higher viscosity of the sample. All spectra were typically acquired with 2048 complex data points in the t2 dimension and 512 points in the t1 dimension. The comparisons of protein chemical shifts and NOE effect were based on the data obtained by two-dimensional NOESY experiments and previous chemical shift assignments (*53*, *54*). Spectral processing was done by applying a sine squared window function in both dimensions followed by zero-filling to 1024 points in the t1 dimension. The chemical shift was referenced to 4,4-dimethyl 4-silapentane sodium carboxylate at 0.015 ppm, and the chemical shifts reported in this study have been deposited in the BioMagnetic Resonance Bank (entry: 15305 for CTX A3 and 15309 for CTX A5). Data processing was done on a Silicon Graphics O2 work station using the XWINNMR program.

SGC Head Group Conformation Analysis. To simplify the spectra, the DPC used for this experiments are deuterium labeled, and the samples were dissolved in 100% D_2O to enable us to observe all the resonances from the SGC head group that are located near water resonances. *J*-coupling values were obtained from DQF-COSY experiments, and distance correlations between head group and interface region of SGC were obtained from 2D-NOESY (100 ms mixing time) experiments.

Head group orientation of SGC is primarily determined by the conformation of the linkage between Gal3S and the ceramide moiety (torsion angles: ϕ, φ, $\theta 1$, $\theta 3$ as depicted in Figure 4B, *55*−*59*). To determine ϕ, φ angles, we focused on 2D NOESY spectra to derived NOE between H1′−H1a and H1′−H1b proton pairs. The diastereotopic protons H1a (downfield) and H1b (upfield) are assigned to the *pro-S* and *pro-R* positions respectively (*58*). The distance between H1′−H1a and H1′−H1b protons is affected by the conformations about C1′−O1 (ϕ) and O1−C1 (φ), which can be measured by its relative NOE effects. Different combinations of ϕ/φ angles result in three types of distance correlation between H1′−H1a and H1′−H1b protons; the first two unique types are shown in Figure 4A. When $\phi/\varphi = -sc/ap$, the distance between H1′ and H1b is always smaller than distance between H1′ and H1a; and when $\phi/\varphi = sc/ap$, the distance between H1′ and H1b will be almost equal to the distance between H1′ and H1a or in other words the NOE intensity between H1′−H1b and H1′−H1a will be equal. The third less unique type (not shown) could be applied to the rest of the combinations of ϕ/φ angles showing the reverse distance correlation as the first type (distance between H1′ and H1b always larger than distance between H1′ and H1a).

Conformation of $\theta 1$ rotamer can be determined by either NOE intensity between H2−H1a and H2−H1b, while the conformation about the C2−C3 bond ($\theta 3$) can be simply determined from the magnitude of coupling between the H2−H3 proton pair (*58*).

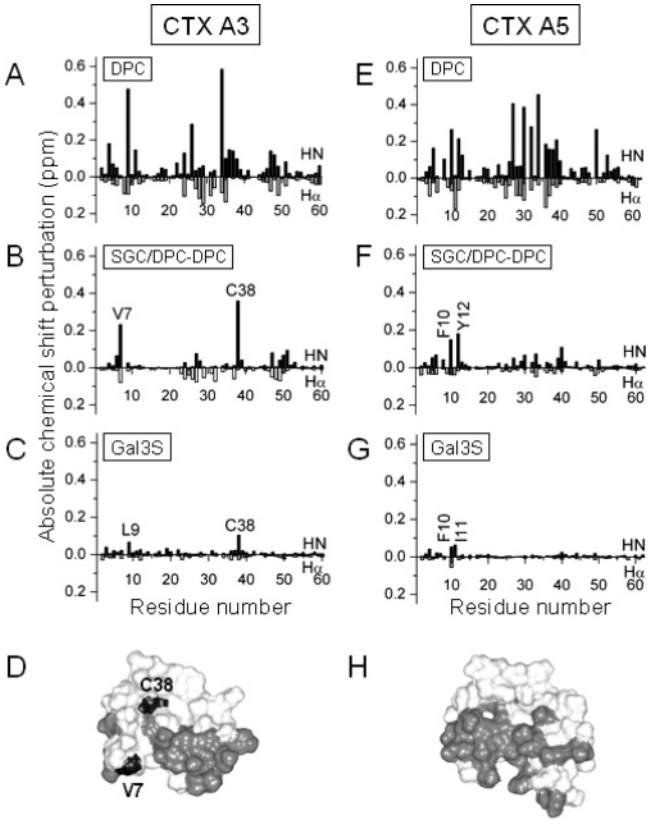

FIGURE 3: Binding site of SGC as revealed by NMR chemical shift perturbation experiments. Absolute chemical shift perturbation on NH and Hα main chain protons of CTX A3 (left) and CTX A5 (right) induced by various types of micelles relative to in 10 mM phosphate buffer (A, B, E, F) or Gal3S (C,G) are presented as a function of amino acid residue position number. The panels B and F depicted as SGC/DPC−DPC represent the absolute chemical shift perturbation difference by subtracting the perturbation induced by 10% SGC/90% DPC micelle to that induced by pure DPC micelle. Residues of major perturbation ($\Delta\delta \geq 0.1$ ppm) as induced by micelle were depicted using surface model (D, H). Gray region shows perturbation region induced by both pure DPC micelle and 10% SGC/90% DPC mixed micelle, and black region shows extra perturbation region induced by 10% SGC/DPC mixed micelle.

Intermolecular NOEs of SGC/CTX. To observe both resonances of SGC and DPC and at the same time to simplify the spectra, 50 mM micelles used for this purpose were prepared by mixing 10% SGC/10% DPC/80% d_{38}-DPC. The identification of CTXs, SGC and DPC proton chemical shifts were based on the data obtained by 2D NOESY experiments and previous chemical shift assignments (*53*, *54*, *60*). Two 1D slices of corresponding resonance bulk methylenes $(CH_2)_n$ and interface proton H3 of SGC were extracted from $\omega 1$ dimension at 1.3 and 4.08 ppm respectively to help to identify the intermolecular NOEs between CTX and lipid tail and SGC interface.

Molecular Modeling of CTX A3/SGC Complex. Starting conformation of SGC was generated from X-ray structure of galactosylceramide (GalCer), determined previously by Pascher and Sundell (*61*), with 3OH′ modified with a sulfate group. Modification on head group dihedral angles was done on InsightII. Complex modeling was conducted using the Discover 3 module from InsightII on a SGI O2 workstation. The AMBER force field with the Homans addition (*62*) and

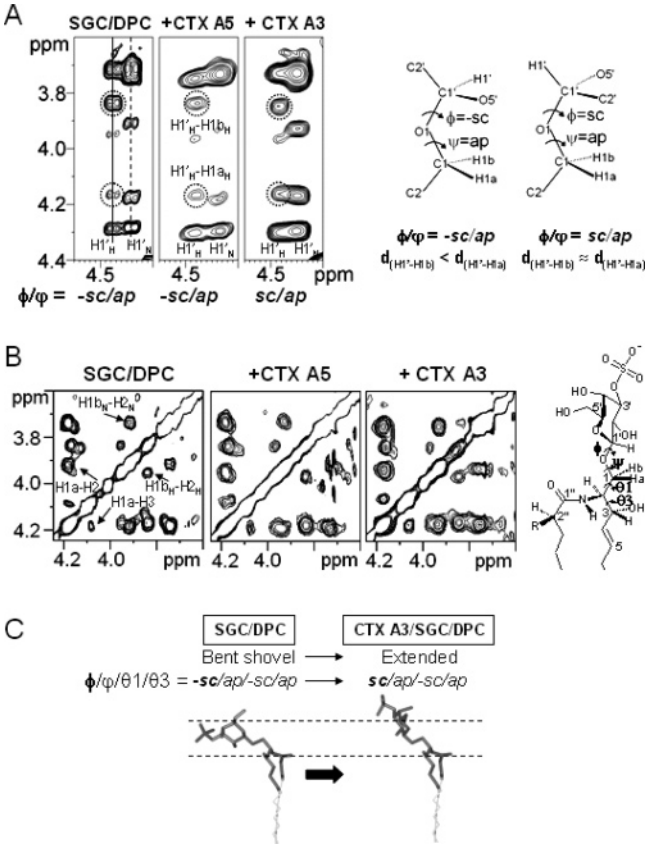

FIGURE 4: 2D-NOESY spectra slices of 10% SGC/DPC mixed micelle in the presence and absence of the designated CTXs for the determination of ϕ/φ (A) and $\theta1/\theta3$ (B) conformation of SGC headgroup (C). In panel A, $H1'_H-H1b_H$ and $H1'_H-H1a_H$ NOE cross peaks were circled by dashed line and assigned accordingly. The relationship between the distance of the designated protons and the angles of ϕ/φ conformation are also shown in the schematic diagram. The definition of the SGC head group conformations: $\phi/\varphi/\theta1/\theta3$ are shown on the right side of panel B with ϕ, O5′−C1′−O1−C1; ψ, C1′−O1−C1−C2; $\theta1$, O1−C1−C2−C3; and $\theta3$, C1−C2−C3−C4 defined according to the nomenclature of Klyne and Prelog (*55*). Schematic diagram to indicate the CTX A3-binding induced conformational change of SGC head group from initial bent shovel conformer into a more extended conformation is shown in panel C. The Gal3S head group of the CTX A3 bound form can be seen to protrude more into aqueous solution than that of the bent shovel conformation.

sulfate parameter extension (*63*) for saccharide was chosen to define the charge distribution and interaction energies in all calculations. Short fatty acid chain mimetic of SGC in its bound conformation to CTX A3 was docked on the predicted binding site of CTX A3 manually. Dielectric constant $\epsilon = 4$ was used to account for dielectric properties of a lipid bilayer at level of saccharide-ceramide linkage (*57*). An energy minimization with 300 steps was performed initially to remove improper atom contacts and forces. A 50 ps molecular dynamics simulation was performed with a time step of 1 fs, and the coordinates of the complex were saved in a trajectory file for the final analysis.

RESULTS AND DISCUSSION

Specificity of CTX A3-Induced Leakage of Vesicles. CTX A3 and CTX A5 are P-type cardiotoxins (Figure 2A amino acid sequence comparison) known to bind peripherally to both zwitterionic PC and acidic PS or PG lipid bilayer (*26, 31*). We have previously demonstrated that CTX A3 can induce detectable lytic effect on both pure PS, pure PG and PS or PG containing POPC vesicle (*31*); however, no significant lytic effect can be observed by CTX A5 on similar lipid preparation, consistent with the noncytotoxic property of CTX A5 (*32*). By using the same approach, we herein compared CTX A3 and CTX A5 effect on membrane containing SGCs (Figure 2). As shown in Figure 2B, CTX A3 induces a more significant effect, up to 70% leakage of total fluorescence content of 6-CF trapped in the large unilamellar vesicles, than CTX A5 (∼20%) on SGC/POPC membrane vesicle. Since CTX A3-induced leakage of pure POPC or POPG/POPC vesicles is observed to be negligible or below 20%, the result also indicates that CTX A3−SGC interaction is indeed specific as we demonstrated previously by patch−clamp and whole cell electrophysiological study on the plasma membrane of cardiomyocytes (*30*).

CTX A3/Sulfatide Pore Formation. To examine whether membrane pore formation of CTX A3, rather than a general lytic action by disrupting the bilayer structure, indeed occurs for SGC containing membrane vesicles, the specificity of CTX-induced leakage was checked by cotrapping fluorescence probe with different molecular size such as dextran probe of FD-70 ($M_w = 50.5$ kDa) and FD-4 ($M_w = 4.4$ kDa). Gel filtration chromatography was used to determine the amount of CTX-induced leakage of dextran probes as shown in Figure 2C. While most of FD-4 can be released from the vesicles after CTX A3 treatment as reflected by the fluorescence intensity relative to the total amount of trapped molecule, FD-70 appeared to remain trapped inside the vesicles and eluted mainly at void volume position. The result strongly suggests that CTX A3-induced leakage indeed is due to the CTX A3 pore formation in SGC containing vesicles. A general lytic action of CTX A3 would induce leakage of FD-70 and FD-4 with similar amount (*64*).

Pore Size. By comparing the retention ratio between FD-4 and FD-70 as a function of CTX A3 concentration (Figure 2D), it is possible to determine the selectivity of the CTX A3/SGC pore formation and yield useful information about the pore size and stability. For instance, the selectivity value of CTX A3-induced pore as determined by extrapolating to zero CTX concentration can be estimated to be 4.5, which was comparable to that of the melittin effect on POPC vesicles (*46*) and significantly larger than the value of 1.8 determined previously for the action of CTX A3 on POPS vesicles (*32*). This result implies that the size or lifetime of the CTX-induced pore in SGC containing vesicles is much smaller or shorter than that in POPS vesicles. We have previously set a lower and upper limit for CTX A3 pore size in POPS vesicles between 20 Å and 100 Å in diameter (*32*). While melittin/POPC pore of 25−30 Å was estimated based on the differences in short and long axis lengths of prolate ellipsoids FD-4 and FD-70, pores of this aperture enable a relatively free passage of FD-4 while reducing significantly the leakage of FD-70 (*46*). Since the selectivity of the CTX A3/SGC pore is similar to that of the melittin/POPC pore, the size of the CTX pore should also be comparable with the estimated value of about 25−30 Å in diameter (Figure 2C). This value is also consistent with the single channel conductance of 18.9 pS for the SGC-dependent CTX A3-induced single channel activity using an outside-out patch of H9C2 cell membranes (*30*).

Pore Lifetime. It is possible to estimate the lifetime of CTX A3 pore formation in SGC containing vesicles by studying the dequenching process of lipid vesicles with entrapped fluorescence CF (*49*). This approach takes advantage of the nonfluorescent quenched CF dimer trapped inside vesicles, in contrast to fluorescent CF monomer after leak out. If the efflux of the encapsulated probe behaves as "all-or-none" when the individual liposomes have either retained all CF marker or lost it totally, it will be indicated by a lack of dequenching of dye remaining inside the vesicles as shown by the theoretical flat broken line in Figure 2E. For a graded efflux (*65*), an internal transient quenching is gradually reduced over the course of time as predicted by the upper broken line in a plot of transient quenching factors Q_t versus the measured efflux function $E(t)$ due to the distribution of partially depleted liposome (Figure 2E). In this regard, vesicles with 50% SGC behave more like "all-or-none" than 100% POPS vesicles since only a slight variation can be observed in the former preparation as shown in the solid line representing data obtained from 50% SGC vesicles. Assuming that the pore sizes of the vesicles fall in the range between 25 and 30 Å, it is estimated that the open lifetime of the pore will have to be longer than theoretical lifetime of about 1−3 ms to account for the observed "all-or-none" leakage of the fluorescence probe. The estimated lifetime of the CTX A3 pore formed in SGC containing vesicle is thus comparable to the lifetime of the SGC-dependent single conductance, i.e., 10−30 ms, as determined by patch−clamp experiment (*30*).

Sulfatide-Induced CTX Oligomerization. We have previously demonstrated that CTX A3-induced leakage of membrane vesicles requires membrane-induced toxin oligomerization in the presence of anionic PG and PS according to the fluorescence energy transfer experiment (*32*). The oligomerization effect is, however, less pronounced for CTX A5, suggesting the requirement of more extended oligomerization during the pore formation process. A similar effect can also be observed for vesicles containing SGC, demonstrating that SGC produced a faster decrease of fluorescence intensity of rhodamine-labeled CTX (Rh-CTX) when Rh-CTX is diluted with intrinsic CTX (Figure 2F). Apparently, despite the stronger binding of CTX A5 to SGC containing micelles (Figure 2G), a lesser degree of CTX A5 oligomerization than CTX A3 may be responsible for the significant effect of CTX A3-induced membrane leakage. Interestingly, the presence of 10% SGC in LPC micelles induce about 2.5-fold increase in the Tyr intrinsic fluorescence of CTX A3 from a saturation level of ∼0.2 to that of 0.5 (Figure 2G, solid line), while the Tyr intrinsic fluorescence of CTX A5 remains similar at ∼0.7 in the presence and absence of SGC (Figure 2G, broken line). Since Tyr 11, Tyr 22, and Tyr 51 in CTX A3 are all located right above the continuous hydrophobic region of CTX A3 responsible for its lipid binding activity (Figure 1), the result further suggests that SGC induces a deeper penetration of CTX A3 molecule into the phospholipid interface. Additional evidence to support the conclusion will be presented later based on the NMR study of CTX A3 and CTX A5 binding to SGC/LPC micelles.

In conclusion, CTX A3 is able to form pores in SGC containing POPC vesicles in a manner similar to the membrane pore formation observed in cardiomyocyte membranes. Despite the higher affinity of CTX A5 toward SGC containing PC micelles than CTX A3, the pore forming activity of CTX A3 is higher. In addition, the CTX A3 pore appears to be more stable in the presence of SGC as compared to other acidic phospholipids of PS and non-cytotoxic CTX A5. To understand how SGC can act differently toward CTX A3 and A5, we first examine whether the two CTXs interact differently with SGC by performing NMR chemical shift perturbation experiments.

Different SGC Binding Site in CTX A3 and A5. Despite that CTX A5 exhibits stronger binding to membrane dispersions than CTX A3 (Figure 2G), CTX A5 induces less membrane leakage than CTX A3 (Figure 2B). Fluorescence spectroscopic measurements also indicate that both CTX A3 and A5 are capable of binding to zwitterionic LPC and negatively charged SGC/LPC micelles. But the Tyr intrinsic fluorescence of CTX A3 undergoes a more significant intensity change than that of CTX A5. In order to examine more specifically how SGC interacts with CTX A3 and A5, we monitored the backbone NH and αH proton chemical shift of CTX A3 and A5 (Figure 3) in the presence of DPC (Figures 3A and 3E), SGC/DPC (Figures 3B and 3F) micelles and SGC headgroup moiety of Gal-3-sulfate (Gal3S, Figures 3C and 3G). The results are then presented as absolute chemical shift perturbation to shed light on the region exhibiting the binding-induced structural change on the CTX molecules.

The binding of DPC micelle toward CTX A3 produce significant 1H chemical shift variation of both αH and NH of 4−12, 22−38, and 47−51 residues which are located at regions near the tip of loops I, II, and III, respectively (Figure 3D). This is consistent with the previous CTX-lipid membrane binding studies for CTX A3/LPC micelle (*43*), CTX *γ*/DPC micelle (*40*), and CTX O2/DPC micelle (*41*), reconfirming that all three hydrophobic loops of P-type CTXs are involved in lipid−CTX interaction. Interestingly, when SGC was introduced into the DPC micelles, it introduced an additional NMR chemical shift perturbation ≥0.2 ppm for residues such as Val 7 and Cys 38 (Figures 3B, 3D). In fact, two additional NOEs are also observed near Cys 38 and three NOEs at Val 7 (Figure 1B emphasized by blue dashed lines at designated residues) as a result of SGC binding. Since these two perturbed residues are located at the same region where Gal3S and heparin mimetics bind (Figure 3C, *44*, *66*), the result suggests that the headgroup moiety of SGC interacts at the core region of CTX A3. It is located at a region near Cys 38 amino acid residue similar to those reported previously for CTX A3/heparin complex structure (*44*, *66*).

When a similar experiment was repeated for CTX A5, as seen in the right panels of Figure 3, the additionally perturbed residues were found at the loop I region (Figures 3F, 3G) albeit CTX A5 also bound to DPC micelles by using the same three hydrophobic tips of the loops in CTX A3 (Figures 3E, 3H). This result suggests strongly that, while the headgroup of SGC binds to CTX A3 at the anionic binding pocket located nearby Cys 38, it binds to CTX A5 at Phe 10, Ile 11, and Tyr 12 closer to the tip of loop I.

The observed different binding site of SGC headgroup between CTX A3 and CTX A5 provides a simple explanation on the larger extent of SGC-induced Tyr fluorescence intensity increase of CTX A3 (Figure 2G). The peripheral

binding mode and penetration depth of CTX on phospholipid membranes have been studied by a combined FTIR and computer simulation approach (*31*). CTX A3 was shown to peripherally bind to both zwitterionic and anionic monolayers in a similar edgewise manner with a tilted angle of 48° between the β-sheet plane of CTX molecule and the normal of the membrane surface (*31*). This binding orientation would allow Cys 38 to be located right above the lipid headgroup region. With the additional help of SGC headgroup specific interaction near the region, CTX A3 molecule will be able to penetrate deeper into the lipid bilayer to enhance significantly on the intrinsic fluorescence intensity of three aromatic Tyr residues located at the interface of lipid bilayers (Figure 1A). In contrast, SGC interact with CTX A5 near the tip of loop I region and can only slightly enhance the binding of CTX A5 with SGC/DPC micelles without significant change on the saturation level of the observed fluorescence intensity change. The differential binding of CTX A3 and A5 to SGC headgroup therefore provides an interesting case to investigate whether SGC headgroup moiety also adapts differently in CTX−SGC interaction and its pore forming activity.

NMR Study on Sulfatide Headgroup Conformation. Sulfatide consists of both α-hydroxylated fatty acids (HFA-SGC) and non-hydroxyl fatty acids (NFA-SGC) with the ratio between NFA and HFA at approximately 1:0.3−0.8 (*45*) for those purified from porcine brain. Special care was therefore taken to assign the HFA-SGC and NFA-SGC proton resonances for the determination of headgroup conformation. As in other glycosphingolipids, orientation of Gal3S is primarily determined by the conformation of the linkage between Gal3S and the ceramide moiety (torsion angles ϕ, φ, θ1, θ3 depicted in Figure 4B, *55*−*59*). Bruzik et al. have determined the headgroup conformation of galactocerebroside based on vicinal coupling constant and NOE intensity measurements (*58*). Since SGC and galactocerebroside only differ in the sulfate group present at the 3′-OH position of SGC, we adopt a similar approach to characterize the SGC headgroup conformation. To determine the ϕ and φ angles, we focused on 2D NOESY spectra to derived NOE between H1′−H1a and H1′−H1b. As shown in Figure 4A, the H1′ proton of NFA-SGC and HFA-SGC are well separated and enable us to determine their respective ϕ, φ angles. Since the $H1b_N$ resonance overlaps with the $H5'_N$ resonance of Gal3S in NFA-SGC, only the headgroup conformation of HFA-SGC will be characterized in this study.

The diastereotopic protons H1a (downfield) and H1b (upfield) are assigned to the *pro-S* and *pro-R* positions respectively (*58*). The distance between H1′−H1a and H1′−H1b protons is affected by the conformations about C1′−O1 (ϕ) and O1−C1 (φ), which can be measured by its relative NOE effects (Figure 4A). For instance, as indicated by the schematic diagram shown on the right-hand side panel of Figure 4A, when $\phi/\varphi = -sc/ap$, the distance between H1′ and H1b is smaller than H1′−H1a. In contrast, when $\phi/\varphi = sc/ap$, the distance between H1′ and H1b is about equal to that between H1′ and H1a. It is therefore possible to determine whether the ϕ/φ angle undergoes conformational change in the presence and absence of CTXs (Figure 4C). With this background in mind, we show in the left panel of Figure 4A that an NOE cross peak of $H1'_H-H1b_H$ (∼6.47) is about 3-fold more intense than that of $H1'_H-H1a_H$ (∼2.18) for SGC/DPC micelles, indicating that $d_{(H1'-H1b)} < d_{(H1'-H1a)}$ for ϕ/φ angles with preferred conformation of $-sc/ap$.

Table 1: Vicinal Proton Coupling Constants (in Hz) of SGC Involved in θ1 and θ3 Conformation Determination at 10% SGC/DPC Mixed Micelle Condition with/without the Presence of CTX A3 (1/5/45) and CTX A5 (1/5/45) at pH = 6.0 and Temperature of 318 K[a]

	HFA			NFA		
	$J_{1a,2}$	$J_{1b,2}$	$J_{2,3}$	$J_{1a,2}$	$J_{1b,2}$	$J_{2,3}$
SGC/DPC micelle	4.55	nd[b]	9.70	4.15	nd	10.24
CTX A3/SGC/DPC	nd	nd	11.20	nd	nd	11.31
CTX A5/SGC/DPC	nd	nd	11.72	nd	nd	10.28

[a] Measured by DQF-COSY at 318 K and 100% D_2O, with estimated error of ±2.9 Hz (under experimental condition of spectral width of 6 kHz, at digital resolution 2048 points). [b] Not determined.

The conformation of θ1 rotamer can be determined by comparing the NOE intensity between H1a−H2 and H1b−H2. As shown in Figure 4B, the H1b−H2 cross peaks of NFA (i.e., $H1b_N-H2_N$) and HFA (i.e., $H1b_H-H2_H$) are well resolved, but the H1a−H2 of both NFA and HFA overlap severely. Therefore, we can only refer the cross-peak intensity of H1a−H2 and H1b−H2 based on the total intensity exhibited by both NFA and HFA. Since strong and equally intense cross peaks between H1a−H2 and H1b−H2 are observed in the presence and absence of CTX A3 and A5, it is suggested that θ1 may adopt $-sc$ conformation for both CTX free and CTX bound SGC/DPC mixed micelle. We are not able to measure the J coupling value of $J_{1a,2}$ and $J_{1b,2}$ to derive the θ1 conformation as shown previously by Bruzik et al. (*58*) probably due to the experimental condition used in this study not being able to resolve J coupling constant smaller than 3 Hz. However, the implicated small value of both $J_{1a,2}$ and $J_{1b,2}$ under the experimental condition is consistent with the $-sc$ conformation for θ1 (Table 1).

To complete the determination of SGC headgroup conformation, the C2−C3 bond (θ3) can be estimated to mainly adopt *ap* conformation as judged from the large J coupling value of ∼9.7 Hz between H2 and H3 proton (Table 1, *58*). It is therefore concluded that the predominant conformation of SGC in 10%SGC/DPC mixed micelle ($\phi/\varphi/\theta1/\theta3$) is −sc/ap/−sc/ap, consistent with the well-established bent shovel conformation of galactosylceramide (GalCer) X-ray crystal structure as also shown in the left-hand side diagram of Figure 4C (*61*, *67*). In fact, this conformation appears to be quite stable since SGC monomer in chlorofrom solution also adopts the same conformation (data not shown). Bent shovel conformation is known as one of the conformations of the lowest energy of GalCer and GlcCer calculated by MM2 and MM3 calculations respectively (*57*, *68*). Sphingomyelin and GalCer also adopt this conformation as observed by NMR (*56*, *58*).

CTX A3-Induced Sulfatide Headgroup Conformational Change. After establishing the preferred SGC headgroup conformation in micelles, we can then determine whether CTXs binding to SGC will induce its conformational change. As shown in Figure 4A, NOESY spectra of CTX A3 binding to 10%SGC/DPC micelle at molar ratio (1:50) show an NOE cross peak of $H1'_H-H1b_H$ (∼6.13) with almost equal intensity of NOE cross peak of $H1'_H-H1a_H$ (∼6.46); while no such effect can be observed for CTX A5. The result

suggests that $d_{(H1'-H1b)} \approx d_{(H1'-H1a)}$ with preferred ϕ/φ angles of *sc/ap* for SGC bound to CTX A3. It should be noted that the $\theta 1$ and $\theta 3$ conformation remains approximately the same since strong and equally intense cross peaks between H2−H1a and H2−H1b are observed (Figure 4B) and the *J*-coupling constant between H2 and H3 is found to be ∼11 Hz for 10%SGC/DPC micelles in the presence of either CTX A3 or CTX A5 (Table 1). The absence of H2−H3 and H3−H1b cross peaks is also consistent with −*sc*/*ap* conformation of $\theta 1$ and $\theta 3$ angles for 10%SGC/DPC mixed micelle with/without CTXs (Figure 4B).

In summary, the predominant conformation ($\phi/\varphi/\theta 1/\theta 3$) of SGC head group upon CTX A3 binding to SGC/DPC mixed micelle is found to be an extended form of *sc/ap/*−sc/*ap* (see the right-hand side schematic diagram shown in Figure 4C) as compared to the bent shovel form of −*sc*/*ap*/−*sc*/*ap*. The same head group conformation was also observed for α-GalCer or α-glycosphingolipid interacting with CD1d (*69*−*71*). The main difference between CTX free and CTX bound form of SGC conformations is due to the reorientation of β-glycosidic bond (i.e., ϕ angle between C1′ of galactose and O1 of ceramide) to adopt a more extended conformation of SGC head group. It is suggested that the binding of SGC headgroup at Cys 38 located around the core region of CTX A3 may be responsible for the observed conformational change.

Sulfatide-Induced Conformational Change of CTX A3. Based on the SGC-induced chemical shift perturbation of CTX A3, a significant conformational change should occur mainly at the three hydrophobic loop region of CTX A3 interacting with SGC/DPC micelles (Figure 3D). This is indeed observed by 2D NMR NOE experiment, showing a significant NOE connectivity change mainly at the loop I and loop II regions (Figure 1B). For instance, three extra connectivities centered at NH of Val 7 near the loop I can clearly be observed upon CTX A3 binding to SGC/DPC micelles carried out at temperature of 318 K. This is also consistent with the observed chemical shift changes at NH of Val7 for CTX A3 molecules bound to SGC/DPC and DPC micelles (Figure 3B). However, the overall folding topology of CTX A3 should remain the same since most, if not all, of the NOE connectivities observed in the β-stranded region are found to be similar in the presence and absence of SGC/DPC micelles (Figure 1B).

It is interesting to point out that a significant change of the NOE intensity can indeed be observed between NH Tyr 22 and CH Cys 38 and between NH Cys 3 and NH Lys 12 at core region far away from the tips of the three fingered loops (see the two blue dashed lines around Cys 38 in Figure 1B). We interpret these changes as a result of the SGC-induced local conformational changes of CTX A3 by the binding of the SGC headgroup near the Cys 38 region. In fact, similar changes of the NOE intensity have also been observed by the binding of heparin-derived short chain mimetics to CTX A3 near the Cys 38 region (*43*). Such an interaction is possible because a positively charged cluster formed by Lys 12, Lys 18, and Lys 35 surrounding the core region of Cys 38 can serve as an anionic binding site not only for the inorganic phosphate, heparin-derived mimetics and ATP (*66*) but also for SGC head group moiety of Gal3S (Figure 3E).

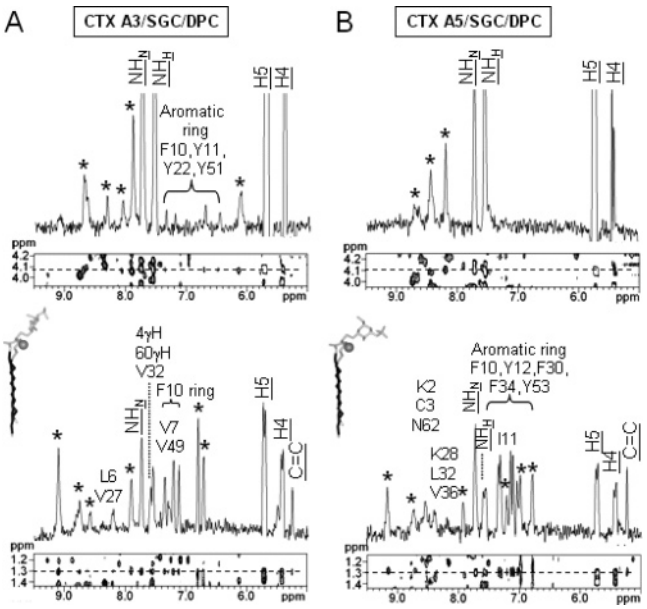

FIGURE 5: Representative 1D and 2D slices derived from 2D NOESY spectra to identify the intermolecular NOEs between SGC and CTX molecules: Top and bottom panels respectively listed the 1D slice at 4.08 ppm for interface proton H3 (gray ball) and 1.3 ppm for methylene $(CH_2)_n$ (black stick) protons of fatty acid chain of SGC molecule. The mixing time of 150 ms and CTX/SGC/DPC/d_{38}-DPC ratio of 1/5/5/40 were used in this study. The asterisk mark of "*" shown on the top of indicated resonances represents the intramolecular NOEs of the CTX molecule itself. Dashed lines in 2D spectra show the location where the 1D slice derived from.

CTX A3/Sulfatide Complex Structure on the Membrane Surface. With the determined CTX A3 bound conformation of SGC molecules and the observed local conformational changes of CTX A3 near the Cys 38 region, it is possible to deduce the SGC−CTX A3 complex structural model if the intermolecular NOE can be observed to allow the docking of SGC headgroup onto the available CTX A3 structure (*32*). We identified intermolecular NOEs between CTXs and lipid from 1D slices of 2D NOESY spectra of corresponding lipid resonances. Based on 1D slice spectra derived from $\omega 1 =$ 4.08 ppm, the H3 interface proton of SGC (marked as a gray ball in the schematic diagram of the SGC structure in Figure 5) was shown to have intermolecular NOEs with aromatic rings of Phe 10, Tyr 11, Tyr 22, and Tyr 51 located at the convex side of CTX A3 (Figure 5A, top panel). It should be noted that the signal at 4.08 ppm of SGC (corresponding to H3 interface proton of SGC) does not overlap with DPC resonances and therefore the effect is mainly due to SGC−CTX interaction.

In contrast, resonances of the methylene proton of SGC/DPC (derived from $\omega 1 = 1.30$ ppm, marked as black stick in SGC structure) show detectable intermolecular NOEs with hydrophobic residues located around the loop region on the convex side of CTX A3. In order to further assign the observed NOE at 1.3 ppm to either the methylene protons of SGC or DPC, we also performed a similar experiment by using micelle samples of CTX A3/SGC/DPC/d_{38}-DPC (molar ratio of 1/5/5/40) and CTX A3/SGC/d_{38}-DPC (molar ratio of 1/5/45). Since a similar NOE effect can also be observed in these samples with perdeuterated DPC micelles, the result indicates that CTX A3 mainly interacts with SGC molecule in mixed micelle.

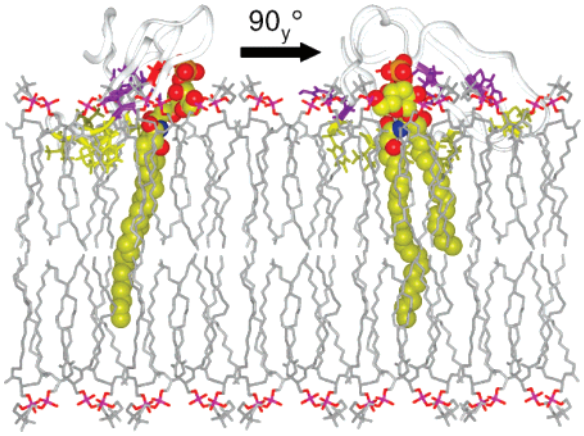

FIGURE 6: Molecular model of CTX A3 binding to SGC molecule in phosphatidylcholine bilayer based on NMR experimental results obtained in this study. Two different views with β-sheet plane of CTX A3 perpendicular (left) and parallel to (right) the paper surface are shown. CTX A3 are represented using ribbon model, with residues showing NOEs with methylene group (yellow stick), NOEs with H3 interface proton of SGC (purple stick), and sulfate binding pocket near Cys 38 (red stick). SGC molecule represented by CPK model is colored as follows: O, red; S, orange; N, blue; C, yellow. DPPC molecules are colored gray except for its phosphate groups, which are colored as P, pink, and O, red.

Taking together all the obtained NMR results, we could build a structural model to describe the peripheral binding mode of CTX A3 with SGC imbedded in PC membrane (Figure 6). For instance, the Cys 38 residue (red) can be located in proximal with sulfate group of SGC and interface H3 proton of SGC be located at about the same height of aromatic residues of CTX A3 (purple) in the peripheral binding mode. The three-fingered hydrophobic loops of CTX A3 can be seen to penetrate into the fatty acyl region of the lipid bilayer (yellow, Figure 6). This is in sharp contrast to the SGC/CTX A3 complex structure determined previously determined by the X-ray method, showing that the three-fingered hydrophobic loops face in opposite direction to the fatty acyl chain of SGC molecule (Figure 7).

If we further consider the anionic binding pocket near the Cys 38 core as a Gal3S binding site, it is possible to dock SGC onto CTX A3 molecule as shown in the left panels of Figure 7. The energy minimized CTX A3/SGC complex structural model indicates that the sulfate group is close to the Cys 38 and stabilized by the anionic binding pocket formed by Lys 12 and Lys 18 near the core. The model is consistent with the additional chemical shift perturbation for the side chains of Lys 12 and Lys 18 observed when SGC molecules are included in DPC micelles for binding study (data not shown). Lys 35 is mainly interacting with SGC molecule at the interface region. Similar degrees of chemical shift perturbation are observed in pure DPC or SGC/DPC micelles. Tyr 22 of CTX A3 appears to form additional hydrogen bonds to the galactose moiety of SGC, as also evidenced by the observed intermolecular NOE. Since Tyr 22 is mutated into Phe 22 in CTX A5, the model also provides a possible explanation why SGC does not bind to CTX A5 at the same region. It is also noted that H3 of SGC does not show a detectable NOE with CTX A5 and the methylene protons exhibit intermolecular NOEs with residues near the loop region of CTX A5 (right panels in Figure 5B), consistent with different binding mode of CTX A5 with CTX A3.

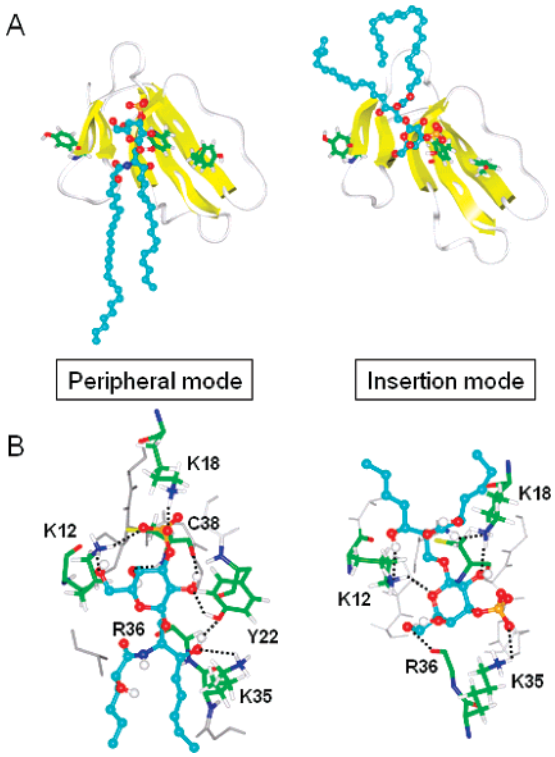

FIGURE 7: Different binding modes of CTX A3/SGC complex structures as determined by NMR and X-ray methods suggesting a role of glycosphingolipid conformational changes to explain the CTX A3 membrane pore forming activities. SGC fatty acid chain points toward loop region of CTX A3 in peripheral binding mode as observed by NMR (left), and fatty acid of SGC points in the reverse direction as shown by X-ray (right). Detailed atomic interactions between CTX A3 and SGC molecules are also shown by the stick model in panel B. The involvement of anionic binding pocket formed by positively charged Lys side chains (Lys 12, Lys 18, and Lys 35) is evident. The interactions of Arg 36 and Cys 38 with SGC are mainly through their backbone. The Tyr 22 side chain of CTX A3 appears to provide an additional H bond for its binding to Gal3S head group moiety of SGC. Hydrogen bonds were shown by black dashed line. Crucial protein residues are colored according to the atom types. SGC molecules are colored as follows: C, cyan; O, red; S, orange; H, white; and N, blue.

Implication to the Pore Formation Model. Despite the details of the model deduced from NMR and molecular docking method, there is no doubt that SGC binds to CTX A3 molecule on membrane surface with Gal3S headgroup close to the Cys 38 core region, H3 of the sphingolipid interface to the aromatic region and fatty acyl chain to the hydrophobic loop region. Such a binding mode may facilitate the deeper penetration of CTX A3 into lipid bilayer without much change of the original orientation of the peripheral binding mode with a tilted angle of ~48° between the β-sheet plane of the CTX molecule and the normal of the membrane surface as determined previously by FTIR and computer simulation approach (*31*, *32*).

In order to form a stable CTX A3 dimer with SGC chelated in between as suggested by X-ray CTX A3/SGC complex structure, both the Gal3S headgroup and the fatty acyl chain will have to undergo global reorientation relative to CTX A3 molecule (see right panels in Figure 7, *30*). The orientations of both SGC and CTX A3 in lipid bilayer are likely to change during the pore formation process if the hydrophobic interaction between CTX A3 and SGC is to be maximized. The SGC headgroup conformation will also

undergo sequential change from CTX free form of *−sc/ap/−sc/ap* to the peripheral mode of *sc/ap/−sc/ap* and then to the insertion mode of *sc/ap/ap/ap* during the process. It has been suggested by Fantini and co-workers that headgroup of glycosphingolipid usually undergoes conformational change to fit the binding site of proteins (*72*). Our results further suggest that such a conformational change is likely to be soft and dynamic since different lipid headgroup conformations are observed even for the same protein binding site. In this regard, our results suggest a scenario that is closer to the recent theoretical simulation for the "distorted toroidal model" with lipid as an essential element to participate as a filler to stabilize the CTX dimer and a facilitator to promote CTX insertion and oligomerization during the pore formation process (*33*).

In summary, the major CTX from Taiwan cobra, CTX A3, is revealed to be able to form transient pore in SGC containing vesicles with properties similar to the pore observed in biological membranes. Although other CTX homologues such as non-cytotoxic CTX A5, a newly identified non-RGD integrin binding proteins of the Ly-6 family (*73*), also bind to SGC, their respective SGC binding site is demonstrated by NMR to be different. A unique property of CTX A3/SGC interaction is the CTX A3-induced change of SGC headgroup conformation. It is suggested that the observed sequential conformational change of SGC plays an important role not only for the initial CTX A3 binding in the peripheral form but also for the SGC-facilitated CTX A3 dimer and oligomer formation to account for the observed transient pore forming activity. SGC is therefore proposed to be an extended part of CTX molecule in its pore forming and membrane translocation activity.

ACKNOWLEDGMENT

We thank Dr. Dennis M. Whitfield, NRC, Canada for kindly providing galactose-3-sulfate (Gal3S); Dr. Fabian Davamani for the kind help in editing the manuscript; and National Synchrotron Radiation Research Center, Taiwan, for the access to beamline 17B2.

REFERENCES

1. Campagna, S., Saint, N., Molle, G., and Aumelas, A. (2007) Structure and mechanism of action of the antimicrobial peptide piscidin, *Biochemistry 46*, 1771−1778.
2. Tilley, S. J., and Saibil, H. R. (2006) The mechanism of pore formation by bacterial toxins, *Curr. Opin. Struct. Biol. 16*, 230−236.
3. Brogden, K. A. (2005) Antimicrobial peptides: pore formers or metabolic inhibitors in bacteria, *Nat. Rev. Microbiol. 3*, 238−250.
4. Kasson, P. M., Kelley, N. W., Singhal, N., Vrljic, M., Brunger, A. T., and Pande, V. S. (2006) Ensemble molecular dynamics yields submillisecond kinetics and intermediates of membrane fusion, *Proc. Natl. Acad. Sci. U.S.A. 103*, 11916−11921.
5. Cohen, F. S., and Melikyan, G. B. (2004) The energetics of membrane fusion from binding, through hemifusion, pore formation, and pore enlargement, *J. Membr. Biol. 199*, 1−14.
6. Kinnunen, P. K., and Holopainen, J. M. (2000) Mechanisms of initiation of membrane fusion: role of lipids, *Biosci. Rep. 20*, 465−482.
7. Balayssac, S., Burlina, F., Convert, O., Bolbach, G., Chassaing, G., and Lequin, O. (2006) Comparison of penetratin and other homeodomain-derived cell-penetrating peptides: interaction in a membrane-mimicking environment and cellular uptake efficiency, *Biochemistry 45*, 1408−1420.
8. Deshayes, S., Morris, M. C., Divita, G., and Heitz, F. (2006) Interactions of amphipathic CPPs with model membranes, *Biochim. Biophys. Acta 1758*, 328−335.
9. Domene, C., Vemparala, S., Klein, M. L., Venien-Bryan, C., and Doyle, D. A. (2006) Role of aromatic localization in the gating process of a potassium channel, *Biophys. J. 90*, L01−L03.
10. Boudker, O., Ryan, R. M., Yernool, D., Shimamoto, K., and Gouaux, E. (2007) Coupling substrate and ion binding to extracellular gate of a sodium-dependent aspartate transporter, *Nature 445*, 387−393.
11. Gouaux, E., and Mackinnon, R. (2005) Principles of selective ion transport in channels and pumps, *Science 310*, 1461−1465.
12. Lacapere, J. J., Pebay-Peyroula, E., Neumann, J. M., and Etchebest, C. (2007) Determining membrane protein structures: still a challenge!, *Trends Biochem. Sci. 32*, 259−270.
13. Law, R. J., Capener, C., Baaden, M., Bond, P. J., Campbell, J., Patargias, G., Arinaminpathy, Y., and Sansom, M. S. (2005) Membrane protein structure quality in molecular dynamics simulation, *J. Mol. Graphics Modell. 24*, 157−165.
14. Fleishman, S. J., Unger, V. M., and Ben-Tal, N. (2006) Transmembrane protein structures without X-rays, *Trends Biochem. Sci. 31*, 106−113.
15. Werten, P. J., Remigy, H. W., de Groot, B. L., Fotiadis, D., Philippsen, A., Stahlberg, H., Grubmuller, H., and Engel, A. (2002) Progress in the analysis of membrane protein structure and function, *FEBS Lett. 529*, 65−72.
16. Teriete, P., Franzin, C. M., Choi, J., and Marassi, F. M. (2007) Structure of the Na, K-ATP*ase* regulatory protein FXYD1 in micelles, *Biochemistry 46*, 6774−6783.
17. Attrill, H., Imamura, A., Sharma, R. S., Kiso, M., and Crocker, P. R., van Aalten, D. M. (2006) Siglec-7 undergoes a major conformational change when complexed with the alpha(2,8)-disialylganglioside GT1b, *J. Biol. Chem. 281*, 32774−32783.
18. Cheever, M. L., Kutateladze, T. G., and Overduin, M. (2006) Increased mobility in the membrane targeting PX domain induced by phosphatidylinositol 3-phosphate, *Protein Sci. 15*, 1873−1882.
19. Kusnetzow, A. K., Altenbach, C., and Hubbell, W. L. (2006) Conformational states and dynamics of rhodopsin in micelles and bilayers, *Biochemistry 45*, 5538−5550.
20. Nyholm, T. K., Ozdirekcan, S., and Killian, J. A. (2007) How protein transmembrane segments sense the lipid environment, *Biochemistry 46*, 1457−1465.
21. Gibbons, W. J., Jr., Karp, E. S., Cellar, N. A., Minto, R. E., and Lorigan, G. A. (2006) Solid-state NMR studies of a diverged microsomal amino-proximate delta12 desaturase peptide reveal causes of stability in bilayer: tyrosine anchoring and arginine snorkeling, *Biophys. J. 90*, 1249−1259.
22. Bond, P. J., and Sansom, M. S. (2007) Bilayer deformation by the Kv channel voltage sensor domain revealed by self-assembly simulations, *Proc. Natl. Acad. Sci. U.S.A. 104*, 2631−2636.
23. Sands, Z. A., and Sansom, M. S. (2007) How does a voltage sensor interact with a lipid bilayer? Simulations of a potassium channel domain, *Structure 15*, 235−244.
24. Haider, S., Khalid, S., Tucker, S. J., Ashcroft, F. M., and Sansom, M. S. (2007) Molecular dynamics simulations of inwardly rectifying (Kir) potassium channels: a comparative study, *Biochemistry 46*, 3643−3652.
25. Dubovskii, P. V., Lesovoy, D. M., Dubinnyi, M. A., Utkin, Y. N., and Arseniev, A. S. (2003) Interaction of the P-type cardiotoxin with phospholipid membranes, *Eur. J. Biochem. 270*, 2038−2046.
26. Chien, K.Y., Huang, W.N., Jean, J.H., and Wu, W. (1991) Fusion of sphingomyelin vesicles induced by proteins from Taiwan cobra (*Naja naja atra*) venom. Interactions of zwitterionic phospholipids with cardiotoxin analogues, *J. Biol. Chem. 266*, 3252−3259.
27. Wu, W. G. (1998) Cobra cardiotoxin and phospholipase A2 as GAG-binding toxins: on the path from structure to cardiotoxicity and inflammation, *Trends Cardiovasc. Med. 8*, 270−278.
28. Vyas, A. A., Pan, J. J., Patel, H. V., Vyas, K. A., Chiang, C. M., Sheu, Y. C., Hwang, J. K., and Wu, W. (1997) Analysis of binding of cobra cardiotoxins to heparin reveals a new beta-sheet heparin-binding structural motif, *J. Biol. Chem. 272*, 9661−9670.
29. Patel, H. V., Vyas, A. A., Vyas, K. A., Liu, Y. S., Chiang, C. M., Chi, L. M., and Wu, W. (1997) Heparin and heparan sulfate bind to snake cardiotoxin. Sulfated oligosaccharides as a potential target for cardiotoxin action, *J. Biol. Chem. 272*, 1484−1492.
30. Wang, C. H., Liu, J. H., Lee, S. C., Hsiao, C. D., and Wu, W. G. (2006) Glycosphingolipid-facilitated membrane insertion and

internalization of cobra cardiotoxin. The sulfatide cardiotoxin complex structure in a membrane-like environment suggests a lipid-dependent cell-penetrating mechanism for membrane binding polypeptides, *J. Biol. Chem. 281*, 656−667.
31. Huang, W. N., Sue, S. C., Wang, D. S., Wu, P. L., and Wu, W. G. (2003) Peripheral binding mode and penetration depth of cobra cardiotoxin on phospholipid membranes as studied by a combined FTIR and computer simulation approach, *Biochemistry 42*, 7457−7466.
32. Forouhar, F., Huang, W. N., Liu, J. H., Chien, K. Y., Wu, W. G., and Hsiao, C. D. (2003) Structural basis of membrane-induced cardiotoxin A3 oligomerization, *J. Biol. Chem. 278*, 21980−21988.
33. Leontiadou, H., Mark, A. E., and Marrink, S. J. (2006) Antimicrobial peptides in action, *J. Am. Chem. Soc. 128*, 12156−12161.
34. Ludtke, S. J., He, K., Heller, W. T., Harroun, T. A., Yang, L., and Huang, H. W. (1996) Membrane pores induced by magainin, *Biochemistry 35*, 13723−13728.
35. Yang, L., Harroun, T. A., Weiss, T. M., Ding, L., and Huang, H. W. (2001) Barrel-stave model or toroidal model? A case study on melittin pores, *Biophys. J. 81*, 1475−1485.
36. Chien, K. Y., Chiang, C. M., Hseu, Y. C., Vyas, A. A., Rule, G. S., and Wu, W. (1994) Two distinct types of cardiotoxin as revealed by the structure and activity relationship of their interaction with zwitterionic phospholipid dispersions, *J. Biol. Chem. 269*, 14473−14483.
37. Prenner, E. J., Lewis, R. N., and McElhaney, R. N. (1999) The interaction of the antimicrobial peptide gramicidin S with lipid bilayer model and biological membranes, *Biochim. Biophys. Acta 1462*, 201−221.
38. Matsuzaki, K., Sugishita, K. I., Harada, M., Fujii, N., and Miyajima, K. (1997) Interactions of an antimicrobial peptide, magainin 2, with outer and inner membranes of Gram-negative bacteria, *Biochim. Biophys. Acta 1327*, 119−130.
39. Chen, T. S., Chung, F. Y., Tjong, S. C., Goh, K. S., Huang, W. N., Chien, K. Y., Wu, P. L., Lin, H. C., Chen, C. J., and Wu, W. G. (2005) Structural difference between group I and group II cobra cardiotoxins: X-ray, NMR, and CD analysis of the effect of cis-proline conformation on three-fingered toxins, *Biochemistry 44*, 7414−7426.
40. Dauplais, M., Neumann, J. M., Pinkasfeld, S., Menez, A., and Roumestand, C. (1995) An NMR study of the interaction of cardiotoxin gamma from *Naja nigricollis* with perdeuterated dodecylphosphocholine micelles, *Eur. J. Biochem. 230*, 213−220.
41. Dubovskii, P. V., Dementieva, D. V., Bocharov, E. V., Utkin, Y. N., and Arseniev, A. S. (2001) Membrane binding motif of the P-type cardiotoxin, *J. Mol. Biol. 305*, 137−149.
42. Chiang, C. M., Chien, K. Y., Lin, H. J., Lin, J. F., Yeh, H. C., Ho, P. L., and Wu, W. G. (1996) Conformational change and inactivation of membrane phospholipid-related activity of cardiotoxin V from Taiwan cobra venom at acidic pH, *Biochemistry 35*, 9167−9176.
43. Sue, S. C., Chien, K. Y., Huang, W. N., Abraham, J. K., Chen, K. M., and Wu, W. G. (2002) Heparin binding stabilizes the membrane-bound form of cobra cardiotoxin, *J. Biol. Chem. 277*, 2666−2673.
44. Sue, S. C., Brisson, J. R., Chang, S. C., Huang, W. N., Lee, S. C., Jarrell, H. C., and Wu, W. (2001) Structures of heparin-derived disaccharide bound to cobra cardiotoxins: context-dependent conformational change of heparin upon binding to the rigid core of the three-fingered toxin, *Biochemistry 40*, 10436−10446.
45. O'Brien, J. S., Fillerup, D. L., and Mead, J. F. (1964) Quantification and fatty acid and fatty aldehyde composition of ethanolamine, choline, and serine glycerophosphatides in human cerebral grey and white matter, *J. Lipid Res. 5*, 329−338.
46. Ladokhin, A. S., Selsted, M. E., and White, S. H. (1997) Sizing membrane pores in lipid vesicles by leakage of co-encapsulated markers: pore formation by melittin, *Biophys. J. 72*, 1762−1766.
47. Lanzetta, P. A., Alvarez, L. J., and Reinach, P. S. (1979) An improved assay for nanomole amounts of inorganic phosphate, *Anal. Biochem. 100*, 95−97.
48. Rex, S., and Schwarz, G. (1998) Quantitative studies on the melittin-induced leakage mechanism of lipid vesicles, *Biochemistry 37*, 2336−2345.
49. Schwarz, G., and Arbuzova, A. (1995) Pore kinetics reflected in the dequenching of a lipid vesicle entrapped fluorescent dye, *Biochim. Biophys. Acta 1239*, 51−57.
50. Runnels, L. W., and Scarlata, S. F. (1995) Theory and application of fluorescence homotransfer to melittin oligomerization, *Biophys. J. 69*, 1569−1583.
51. Sharpe, J. C., and Landon, E. (1999) Diphtheria Toxin Forms Pores of Different Sizes Depending on Its Concentration in Membranes: Probable Relationship to Oligomerization, *J. Membr. Biol. 171*, 209−221.
52. Bax, A., and Davis, D. G. (1969) MLEV-17-based two-dimensional homonuclear magnetization transfer spectroscopy, *J. Magn. Reson. 65*, 355−360.
53. Sue, S. C., Jarrell, H. C., Brisson, J. R., and Wu, W. (2001) Dynamic characterization of the water binding loop in the P-type cardiotoxin: implication for the role of the bound water molecule, *Biochemistry 40*, 12782−12794.
54. Singhal, A. K., Chien, K. Y., Wu, W. G., and Rule, G. S. (1993) Solution structure of cardiotoxin V from *Naja naja atra*, *Biochemistry 32*, 8036−8044.
55. Klyne, W., and Prelog, V. (1960) Description of steric relationships across single bonds, *Experientia 16*, 521−523.
56. Bruzik, K. S. (1988) Conformation of the polar headgroup of sphingomyelin and its analogues, *Biochim. Biophys. Acta 939*, 315−326.
57. Nyholm, P. G., and Pascher, I. (1993) Orientation of saccharide chains of glycolipids at the membrane surface: conformational analysis of the glucose-ceramide and the glucose-glyceride linkages using molecular mechanics (MM3), *Biochemistry 32*, 1225−1234.
58. Bruzik, K. S. (1997) NMR study of conformation of galactocerebroside in bilayers and solution: galactose reorientation during the metastable-stable gel transition, *Biochemistry 36*, 566−575.
59. Li, L., Tang, X., Taylor, G., DuPré, D. B., and Yappert, M. C. (2002) Conformational characterization of ceramides by nuclear magnetic resonance spectroscopy, *Biophys. J. 82*, 2067−2080.
60. Dabrowski, J, Egge, H, Hanfland, P. (1980) High resolution nuclear magnetic resonance spectroscopy of glycosphingolipids. I: 360 MHz 1H and 90.5 MHz 13C NMR analysis of galactosylceramides, *Chem. Phys. Lipids 26*, 187−196.
61. Pascher, I., and Sundell, S. (1977) Molecular arrangements in sphingolipids. The crystal structure of cerebroside, *Chem. Phys. Lipids 20*, 175−191.
62. Homans, S. W. (1990) A molecular mechanical force field for the conformational analysis of oligosaccharides: comparison of theoretical and crystal structures of Man alpha 1-3Man beta 1-4GlcNAc, *Biochemistry 29*, 9110−9118.
63. Huige, C. J. M., and Altona, C. (1995) Force field parameters for sulfates and sulfamates based on ab initio calculations: Extensions of AMBER and CHARMm fields, *J. Comput. Chem. 16*, 56−79.
64. Benachir, T., and Lafleur, M. (1995) Study of vesicle leakage induced by melittin, *Biochim. Biophys. Acta 1235*, 452−460.
65. Pokorny, A., and Almeida, P. F. (2004) Kinetics of dye efflux and lipid flip-flop induced by delta-lysin in phosphatidylcholine vesicles and the mechanism of graded release by amphipathic, alpha-helical peptides, *Biochemistry 43*, 8846−8857.
66. Tjong, S. C., Chen, T. S., Huang, W. N., and Wu, W. G. (2007) Structures of heparin-derived tetrasaccharide bound to cobra cardiotoxins: Heparin binding at a single protein site with diverse side chain interactions, *Biochemistry* (accepted).
67. Pascher, I., Lundmark, M., Nyholm, P. G., and Sundell, S. (1992) Crystal structures of membrane lipids, *Biochim. Biophys. Acta 1113*, 339−373.
68. Nyholm, P. G., Pascher, I., and Sundell, S. (1990) The effect of hydrogen bonds on the conformation of glycosphingolipids. Methylated and unmethylated cerebroside studied by X-ray single crystal analysis and model calculations, *Chem. Phys. Lipids 52*, 1−10.
69. Zajonc, D. M., Cantu, C., Mattner, J., Zhou, D., Savage, P. B., Bendelac, A., Wilson, I. A., and Teyton, L. (2005) Structure and function of a potent agonist for the semi-invariant natural killer T cell receptor, *Nat. Immunol. 6*, 810−818.
70. Koch, M., Stronge, V. S., Shepherd, D., Gadola, S. D., Mathew, B., Ritter, G., Fersht, A. R., Besra, G. S., Schmidt, R. R., Jones, E. Y., and Cerundolo, V. (2005) The crystal structure of human CD1d with and without alpha-galactosylceramide, *Nat. Immunol. 6*, 819−826.
71. Wu, D., Zajonc, D. M., Fujio, M., Sullivan, B. A., Kinjo, Y., Kronenberg, M., Wilson, I. A., and Wong, C. H. (2006) Design of natural killer T cell activators: Structure and function of a microbial glycosphingolipid bound to mouse CD1d, *Proc. Natl. Acad. Sci. U.S.A. 103*, 3972−3977.

72. Fantini, J. (2003) How sphingolipids bind and shape proteins: molecular basis of lipid-protein interactions in lipid shells, rafts and related biomembrane domains, *Cell. Mol. Life Sci. 60*, 1027−1032.
73. Wu, P. L., Lee, S. C., Chuang, C. C., Mori, S., Akakura, N., Wu, W. G., and Takada, Y. (2006) Non-cytotoxic cobra cardiotoxin A5 binds to alpha(v)beta3 integrin and inhibits bone resorption. Identification of cardiotoxins as non-RGD integrin-binding proteins of the Ly-6 family, *J. Biol. Chem. 281*, 7937−7945.

BI700871X